Academic Journal of Science and Technology
ISSN: 2771-3032 | Vol. 14, No. 2, 2025

Pore and Fracture Features Based on CT Scanning

-- A Case Study from The Pingdingshan Coalfield

Junjie Zhao[1, a]

[1]School of Resources and Environment, Henan Polytechnic University, Jiaozuo 454003, China
[a]15670850280@163.com

Abstract: To precisely characterize the pore-fracture architecture of Permian coal samples from Pingdingshan Mine Area 10, X-ray computed tomography (CT) technology was employed for systematic investigation. A dual-method analytical framework integrating qualitative assessment and quantitative metrics was implemented to evaluate pore size distribution, porosity, and connectivity. Three-dimensional CT reconstruction revealed stratified propagation patterns of pore-fracture systems, with mineral components exhibiting pronounced stratification characteristics. Quantitative analysis of pore-throat configurations within the pore network model demonstrated descending orders of average pore radius and throat radius across specimens: SK42 > SS21 > SK21. While SS21 exhibited the broadest throat radius distribution, SK42 displayed the largest mean throat radius with limited developmental frequency. Connectivity coefficients for SS21, SK21, and SK42 measured 0.1266, 0.1061, and 0.023 respectively, indicating superior interconnectivity and structural integrity in SS21 compared to other specimens.

1. Introduction

The methods for characterizing the microstructure of coal pore and fracture systems can be broadly classified into three categories. The first category involves direct observation using optical or electron microscopy. Although this technique allows for non-destructive measurement of the pore and fracture characteristics within the coal, it is limited to two-dimensional representations of these features [1-2].The second category involves injecting specific fluids into the coal, thereby indirectly revealing the characteristics of the pore and fracture structure. Techniques such as N_2 and CO_2 adsorption experiments and mercury intrusion porosimetry fall under this classification [3-5]. These experiments do not directly visualize the pores and fractures but rather infer their volume, shape, and connectivity by analyzing changes in the fluid volume as it enters and exits the coal [6-7]. Moreover, the fluids must be injected under controlled pressures, which can alter the pore structure, and the scale of observation is constrained by the pressure of the fluid [8-9].The third category is the use of ray-based detection methods, where X-ray scattering and wave propagation are employed to comprehensively investigate the features of pores and fractures in coal. X-ray computed tomography (CT) imaging, including steps such as image cropping, grayscale adjustment, filtering, threshold segmentation, three-dimensional reconstruction, and quantitative analysis of porosity and fractures, allows for the three-dimensional visualization of the pore and fracture network. Importantly, this method is non-destructive to the coal structure and has thus gained significant favor among researchers [10-12].

2. Geological Overview of the Pingdingshan Mining Area

The Pingdingshan mining area is located in the central part of Henan Province, China, within the stratigraphic division of the North China stratigraphic region. The coal-bearing strata in the area belong to the Late Paleozoic Permian coal-bearing sequence. From the bottom to the top, the coal-bearing strata consist of the Taiyuan Formation, Shanxi Formation, Lower Shihezi Formation, and Upper Shihezi Formation, with a total of 74 coal seams and a cumulative coal thickness of 18.26 meters. The primary coal seams for coalbed methane development are the No. 2 coal of the second coal section in the Shanxi Formation and the No. 2 and No. 3 coals of the fourth coal section in the Lower Shihezi Formation, which are also the focus of this study. The generation and occurrence of coalbed methane in the Shanxi and Lower Shihezi coal-bearing sequences are primarily controlled by the peat swamp environment on the tidal flats, delta distributary bay swamp, and distributary channel sedimentary environments [13].

The Pingdingshan mining area is located at the northern edge of the North China Plate, within the Xianxiong tectonic zone, at the forefront of a large NW-trending thrust fault zone. It lies in the transitional zone between the North China Platform and the Qinling Fold Belt. The entire mining area forms an isolated fault-block uplift structure, with the central region elevated and surrounded by depressions. Tectonically, it is characterized by NW-trending fault-fold structures. The primary structural feature of the area is the Likou syncline, with the Shishan No. 1 mine situated on the northern flank of the syncline, and the No. 10 mine located on its NE wing [14-15] (Figure 1).

3. Experimental Samples and Methods

The research subjects of this study are the No. 2 coal from the second coal section, No. 2 coal from the fourth coal section, and No. 3 coal from the fourth coal section of the Shouyi Mine and the Shishi Mine. The samples were all freshly extracted from the underground working faces. Various experiments, including industrial analysis, microscopic component statistics, and micro-CT imaging, were conducted on the coal samples. The reflectance of vitrinite and the microscopic component statistics were performed using a Zeiss Axioskop 40 polarized light microscope (Zeiss, Germany) and an MSP UV-VIS2000 microscopic spectrophotometer (3-Y Corporation, USA). The measurement procedures followed GB/T 8899-2013. The results of the industrial analysis, vitrinite reflectance, and

microscopic component testing of the coal samples are shown in Table 1.

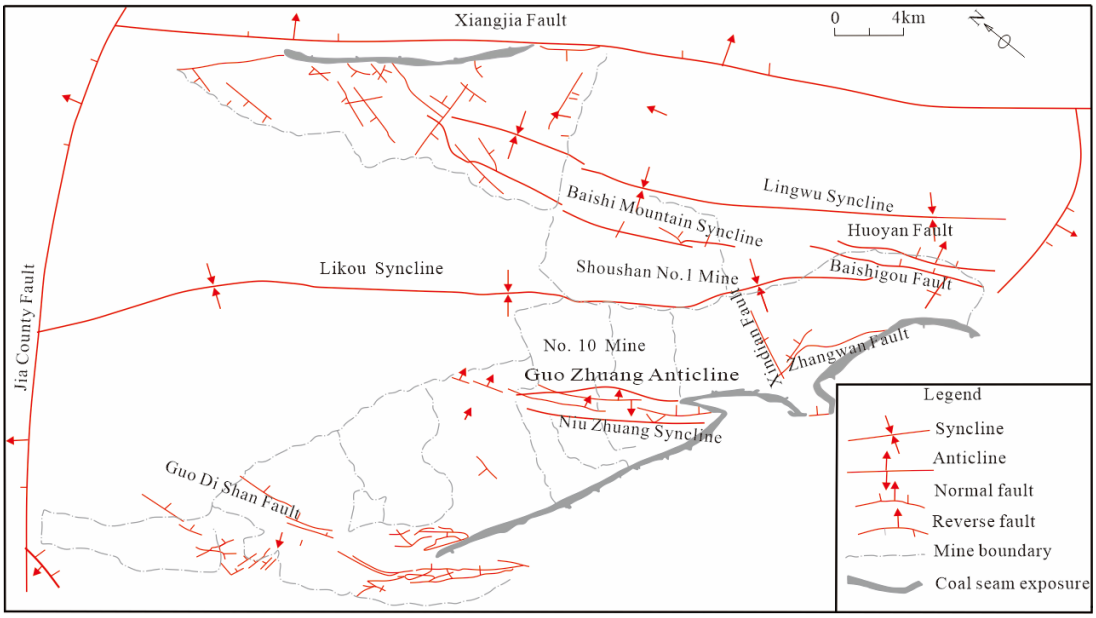

Figure 1. Geological Structure of the Study Area

Table 1. Basic Coal and Rock Quality Data for the Pingdingshan Mining Area (%)

Sample number	Organic microscopic constituents			inorganic mineral	M_{ad}	A_d	V_{daf}	F_{cd}	R^o_{max}
	Vitrinite	Inertinite	Liptinite						
SS21	79.4	20.4	0.2	14.2	0.85	13.22	22.19	69.67	1.56
SK21	81.81	10.11	—	8.08	1.26	14.83	31.38	88.63	—
SK42	73.38	12.23	1.56	12.83	1.11	24.42	31.89	87.06	1.32
SK43	72.45	15.08	4.61	7.86	1.04	27.38	33.43	86.48	1.56

The three-dimensional microstructure scanning of the internal fractures of coal and rock was performed using the V|tome|x S240 industrial CT scanning system (GE Healthcare, USA). The scanning parameters were as follows: tube voltage of 10 to 240 kV, tube current of 0.01 to 3.0 mA, a minimum focal spot size of ≤3 μm, and a resolution of ≤ 2 μm. The coal samples were drilled into coal pillars with a diameter of 25 cm and a length of ≤ 50 cm (Figure 2), and after being dried at a constant temperature of 60 ° C for 24 hours, they underwent 360° X-ray CT scanning to obtain a large number of two-dimensional images. The scanning parameters are listed in Table 2. Using high-performance computers, the acquired two-dimensional slices of the coal samples from the X-ray CT scans were digitally processed using ImageJ and Avizo software. The image processing steps included cropping, grayscale adjustment, filtering, threshold segmentation, and three-dimensional visualization. This process enabled the precise identification and extraction of the distribution features of the fractures and pores within the coal.

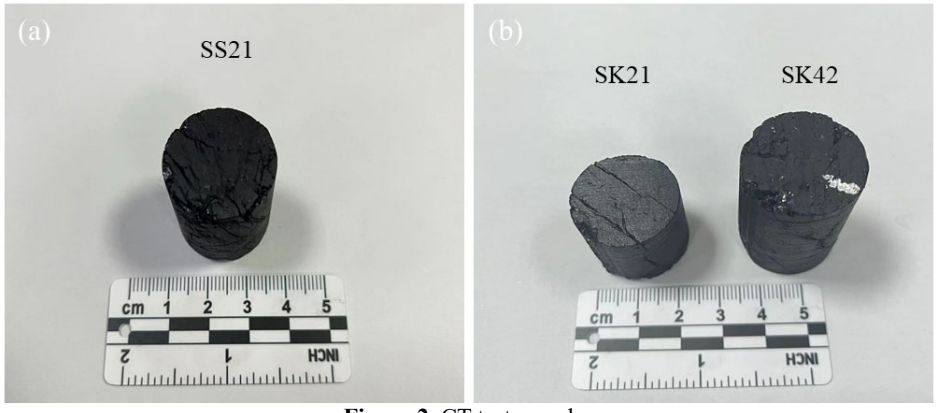

Figure 2. CT test sample.

Image processing steps are as follows:

(1) Image cropping

During sample processing, strict adherence was maintained to the National Standard GB/T 482-2008 and the International Society for Rock Mechanics (ISRM) standards. However, localized damage phenomena were observed at the edges of certain coal pillars (Fig. 3a). During X-ray CT scanning and permeability testing of the coal pillars, edge-damaged areas or surface fractures were typically classified as invalid regions. To ensure experimental accuracy, these invalid

regions were first removed. Valid images (Fig. 3b) were obtained by cropping the invalid regions using the TransformJ plugin for image cropping in ImageJ software.

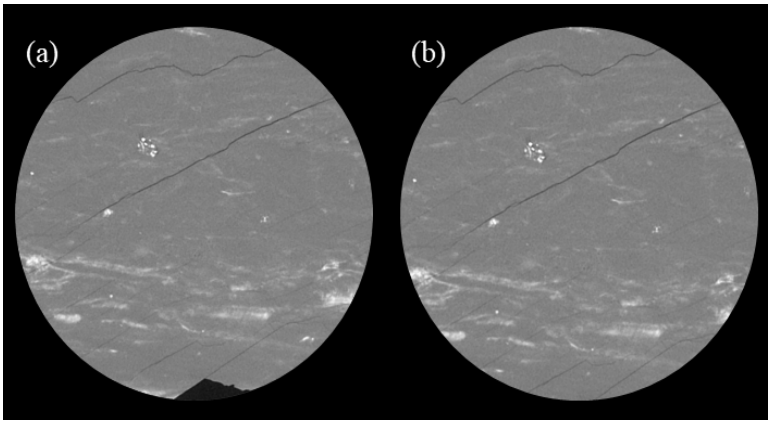

Figure 3. Image cropping

(2) Gray-Level Adjustment

Due to variations in parameter settings during CT scanning, the acquired 2D images may exhibit uneven brightness (e.g., overly dark or bright). These images often require gray-level adjustments to optimize visibility. In this experiment, however, the image brightness remained highly consistent across samples (Fig. 4), eliminating the need for further processing. This uniformity allowed the 3D reconstruction software to clearly visualize and distinguish 2D cross-sectional slices of different regions. As shown in Fig. 4, the three primary components of coal were easily identifiable: white represents mineral constituents, black corresponds to pores/fractures, and gray denotes the coal matrix

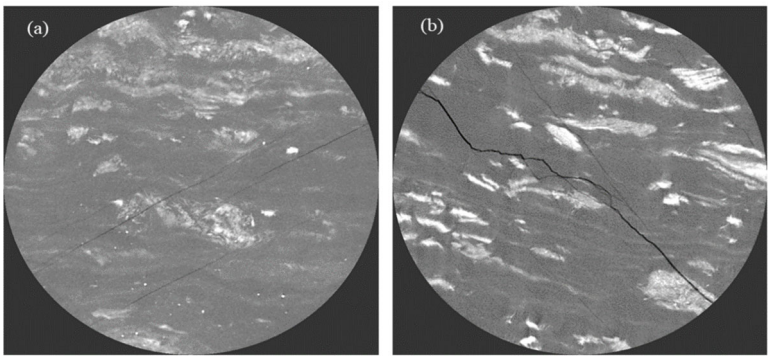

Figure 4. Image Gray-Level Adjustment

(3) Filtering Processing

During X-ray CT scanning, system noise caused by equipment operation or environmental disturbances may introduce black spots, degrading image quality and introducing errors in subsequent 3D reconstruction and quantitative characterization14. Common denoising methods include median filtering, Gaussian filtering, and mean filtering479. In this study, 3D filtering was applied to the images using Avizo software. Figure 5a shows the original image, Figure 5b displays the result after non-local means (NLM) filtering, and Figure 5c demonstrates the effect of median filtering. Comparative analysis revealed that the NLM-filtered image (Fig. 5c) achieved the best performance: the original black spots were eliminated, and the boundaries between coal fractures and the matrix became more natural and distinct910, facilitating subsequent image segmentation and feature extraction tasks

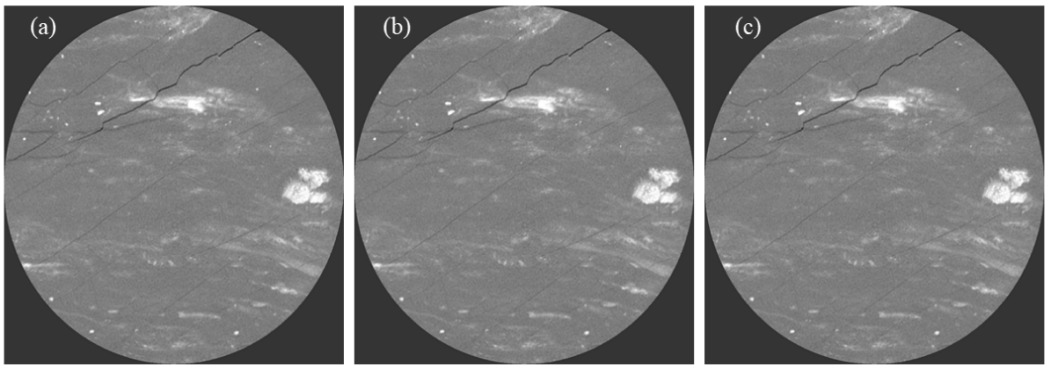

Figure 5. Image filtering Processing

(4) Gray-Level Threshold Segmentation

The 2D images obtained from industrial X-ray CT scanning contain three pixel types: pores/fractures, minerals, and matrix, each exhibiting distinct gray-level characteristics. Precise identification of pores/fractures is achieved by leveraging these gray-level differences, using conventional segmentation algorithms. To more accurately separate pores/fractures from the coal matrix, this study employs the watershed algorithm—a widely adopted method in coal-rock slice analysis—for image segmentation and 3D reconstruction. Figure 6a shows the original coal column image, while Figure 6b displays the segmented result using the watershed algorithm, with fractures marked in blue.

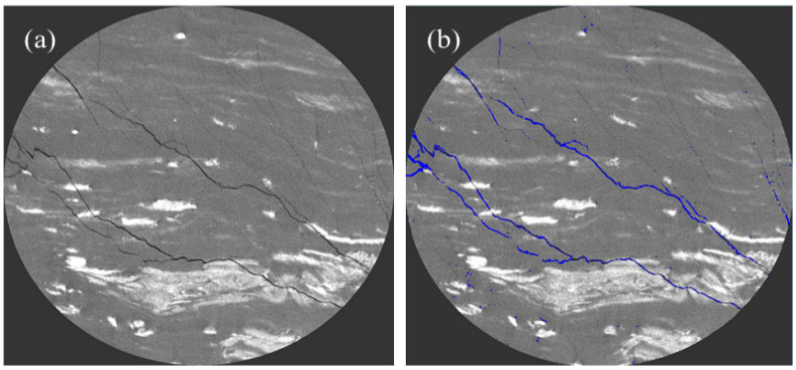

Figure 6. Image Threshold Segmentation

(5) 3D Visualization

The specific parameters for the X-ray CT scanning of the coal column are detailed in Table 2. Using Avizo software, the threshold-segmented 2D images were stacked three-dimensionally to generate a 3D visualization of the coal column's X-ray CT data.

Table 2. Basic parameters of X-ray CT of coal samples

Sample number	diameter /mm	length /mm	resolution /μm	Scan length /mm	Number of slices
SS21	24	32	21.53	32	1000
SK21	23.5	50	27.79	32	860
SK42	23.3	26.5	24.97	26	1000

4. Spatial Structure and Connectivity Characteristics of Coal Pores/Fractures (3D Features)

4.1. Pore/Fracture Characteristics Based on CT Image Recognition

Figure 7 shows a typical 2D slice of the coal sample, where three gray levels correspond to distinct components: white (minerals), gray (coal matrix), and black (fractures). The CT 2D slice clearly reveals a high degree of fracture development in the coal.

While fractures provide pathways for gas seepage, the number of fractures alone cannot directly indicate the effective gas transport space or permeability. Thus, a refined quantitative analysis of fracture aperture distribution and volumetric contribution is essential58. Using Avizo software, fractures were extracted from 2D slices, and their 3D spatial features are displayed in Figure 8. The results indicate concentrated fracture distributions across three coal seams, particularly in samples SS21 and SK21, with uniform aperture distributions

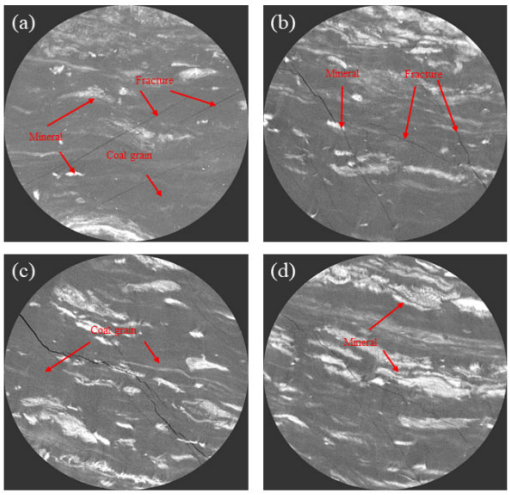

Figure 7. Typical 2D Slices of X-ray CT

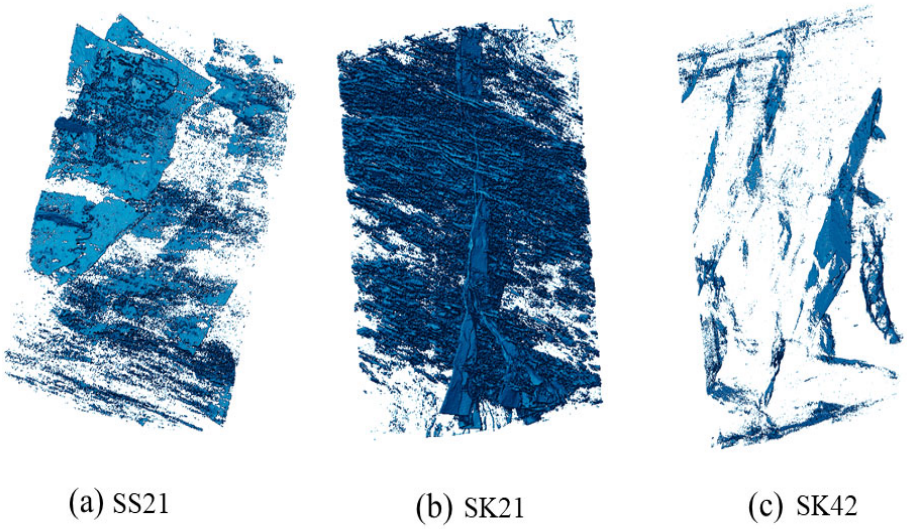

Figure 8. 3D Visualization of X-ray CT Fractures

4.1.1. X-ray CT Fracture Aperture and Volume Distribution

The Avizo software was used to extract and calculate the proportion of fractures of different apertures relative to the total fracture volume, which represents the volume contribution of fractures with different apertures, as shown in Figure 9. For coal sample SS21, fractures with apertures ranging from 0 to 100 μm contribute the largest volume, accounting for 35.9%; for coal sample SK21, fractures with apertures ranging from 0 to 100 μm also contribute the largest volume, accounting for 34.09%; for coal sample SK42, fractures with apertures ranging from 0 to 100 μm contribute the largest volume, accounting for 35.47%. The volume contribution in all three coal samples is mainly from microfractures, with large fractures ranging from 600 to 1000 μm developed in SS21 and SK21, while large fractures are almost undeveloped in SK42.

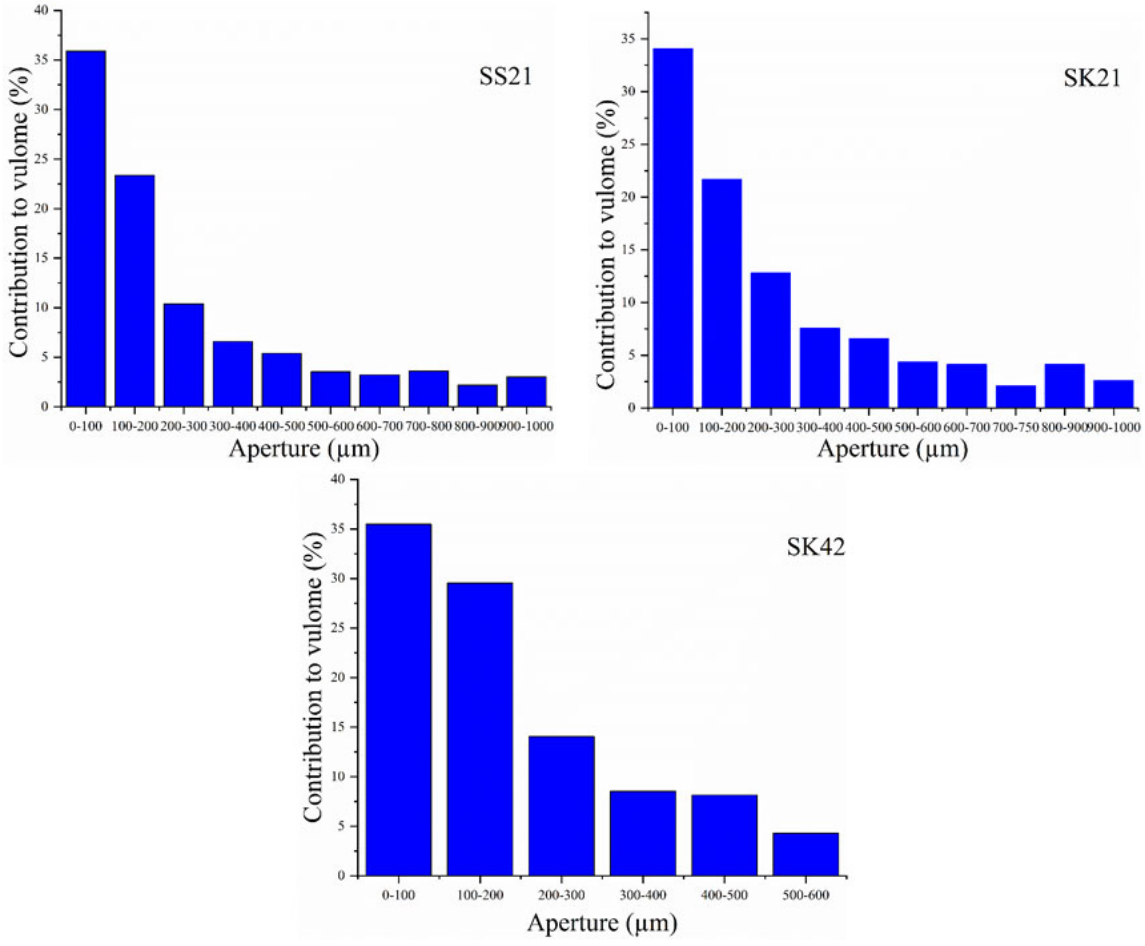

Figure 9. Fracture Volume Contribution of Coal Samples SS21, SK21, and SK42

4.2. Pore Network Model

First, the Separate Objects module in Avizo software is used to segment the fracture space into a set of connected and labeled spheres. Then, the Generate Pore Network Model command in the Avizo XPoreNetworkModeling Extension is employed to establish the pore network model, which is subsequently visualized. The color of the pores is generated based on their volume, while the color of the throats is divided according to their equivalent radius. The resulting complex pore network model is shown in Figure 10.

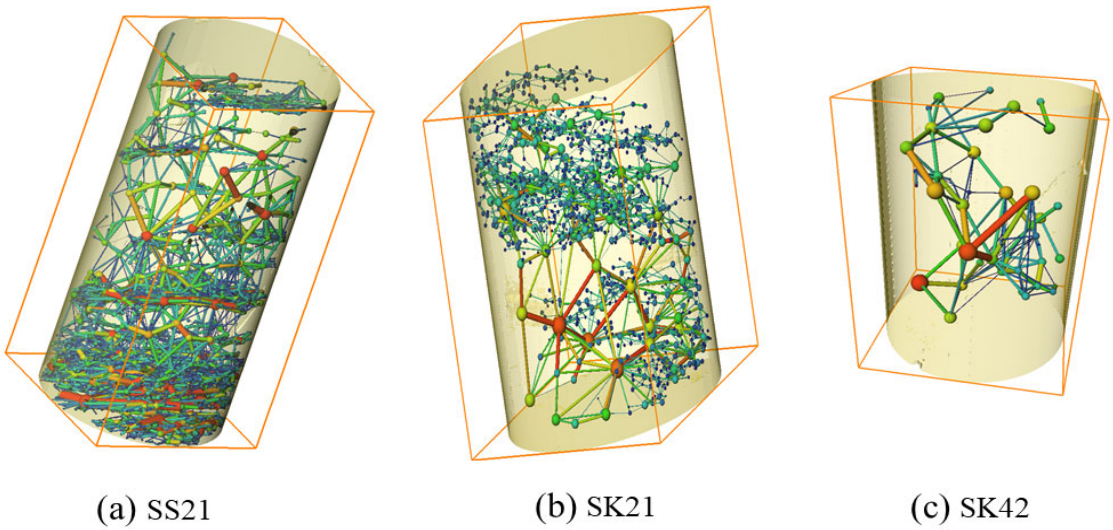

Figure 10. Pore Network Models of Coal Samples SS21, SK21, and SK42

The pore network structural parameters primarily include the number, equivalent radius, and volume of pores, as well as the number, equivalent radius, and length of throats. The results are presented in Table 3. SK42 has the fewest pores, totaling 396, while SS21 has the most, with 3,284 pores. SK42 has the fewest throats, totaling 163, while SS21 has the most, with 5,656 throats. The pore radius ranges from a minimum of 124.02 μm to a maximum of 1,346.68 μm. The pore volume ranges from a minimum of 7,991,070 μm³ to a maximum of 10,230,134,780 μm³. The throat radius ranges from a minimum of 8.66 μm to a maximum of 796.49 μm. The throat length ranges from a minimum of 268.88 μm to a maximum of 15,045.43 μm.For the SS21 coal sample, there are 3,284 pores and 5,656 throats. The pore radius distribution ranges from 124.02 μm to 1,334.92 μm, with an average of 419 μm. The pore volume distribution ranges from 7,991,070 μm³ to 9,964,000,000 μm³. The throat radius distribution ranges from 9.91 μm to 796.49 μm, with an average of 160.03 μm.

Table 3. Structural Parameters of Pore Network Models for Coal Samples SS21, SK21, and SK42

Pore network model		SS21	SK21	SK42
Number of pores/number		3284	3019	396
Number of laryngeal tracts/pcs		5656	2538	163
Pore radius/μm	Min	124.02	124.62	196.2226
	Max	1334.92	1026.844	1346.68
	Average	419	405.71	794.93
Pore volume/μm³	Min	7991070	8106882	31647222
	Max	9960000000	4535260160	10230134780
	Average	515000000	437153204.3	3271691690
Radius of the larynx/μm	Min	9.91	8.66	13.21
	Max	796.49	691.21	491.49
	Average	160.03	155.23	179.59
Radius of the larynx/μm	Min	268.88	268.88	427.08
	Max	8095.5	9511.59	15045.43
	Average	1723.87	1775.52	6085.65

4.2.1. Pore and Throat Structural Characteristics

Figure 11 presents the pore radius distribution of the pore network model for the samples. As shown in Figure 11(a), the pore radius distributions of coal samples SS21 and SK21 are similar. Both samples exhibit multiple peaks, indicating

complex pore network connectivity. Additionally, the equivalent pore diameters of SS21 and SK21 are concentrated between 250 and 550 μm. In contrast, Figure 11(b) reveals that SK42 has larger pore diameters, a broader pore diameter distribution, and more frequent occurrences of multiple peaks compared to SK21, suggesting a more complex pore network connectivity.

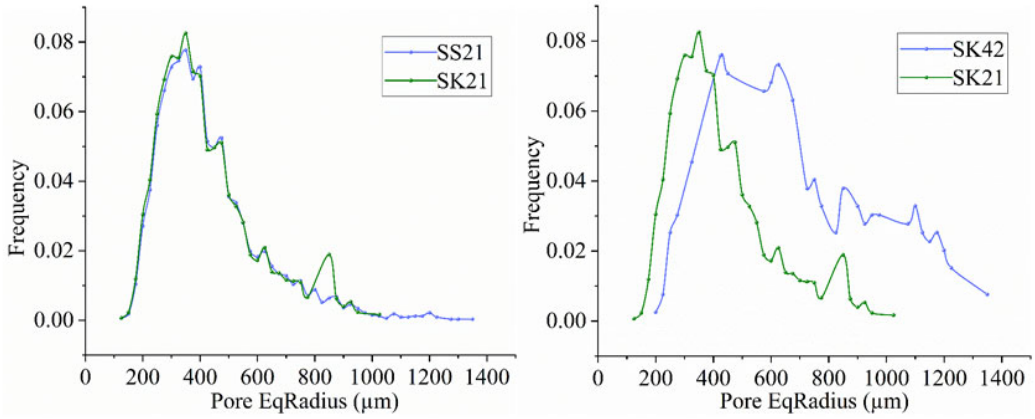

Figure 11. Pore Radius Frequency Distribution of Pore Network Models for Coal Samples SS21, SK21, and SK42

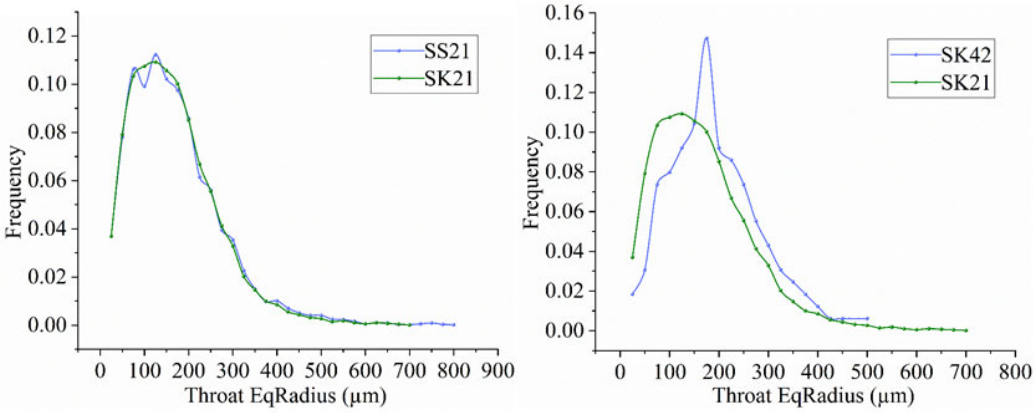

Figure 12. Throat Radius Distribution of Pore Network Models for Coal Samples SS21, SK21, and SK42

Figure 12 illustrates the pore throat radius distribution of the pore network model. The distribution curves for coal samples SS21 and SK21 are similar, indicating comparable connectivity. SK21 exhibits a broader throat radius distribution, while SK42 has a significantly higher throat radius in the 180–500 μm range compared to SK21. Overall, coal samples SS21 and SK21 demonstrate better fracture connectivity.

4.2.2. Pore Fracture Connectivity and Bonding Strength

Coal seam permeability is influenced by multiple factors, including the aperture, spacing, connectivity, and bonding strength of fractures within the coal, as well as the degree and orientation of mineral infill. In this study, a connectivity criterion of 26 is adopted, meaning that connections between objects can be point, line, or surface contacts. The bonding strength in the pore network model is represented by the ratio of pore radius to throat radius. The evaluation formula for three-dimensional connectivity[16-17] is calculated as Equation 1-1:

$$C = \frac{V^1}{V} \qquad (1-1)$$

where C is connectivity, V^1 is the volume of connected fractures, and V is the sample volume.

The formula for bonding strength in the pore network model is given by Equation 1-2:

$$R_{pt} = \frac{l_p}{l_t} \qquad (1-2)$$

where R_{pt} is the pore-throat ratio, l_p is the pore radius, and l_t is the throat radius. $R_{pt} \geq 1$ indicates that the larger the pore-throat ratio, the weaker the bonding strength; conversely, a smaller Rpt indicates stronger bonding strength.

The connectivity and pore-throat ratios of fractures in the samples are shown in Table 4. SS21 exhibits better connectivity than SK21, and SK21 has better connectivity than SK42.Regarding bonding strength, SS21 has stronger bonding strength than SK21, and SK21 has stronger bonding strength than SK42.

Table 4. Connectivity and Pore-Throat Ratio Data for Coal Samples SS21, SK21, and SK42

Sample Number	Connectivity /%	Pore-throat Ratio
SS21	0.1266	2.614
SK21	0.1061	2.618
SK42	0.023	4.426

5. Conclusions

A study on the pore-fracture development characteristics of the No. 1 coal and No. 4-2/4-3 coal reservoirs in the Shoushan-1 and Shikuang-10 mines of the Pingdingshan mining area yielded the following findings:

(1) X-ray CT slices revealed strong heterogeneity and abundant mineral development in coal samples. Fracture extraction via Avizo software showed that micro-fractures in samples SS21, SK21, and SK42 contributed significantly to total fracture volume. However, the volumetric contributions of SK21 and SK42 differed markedly, while SS21 and SK21 exhibited comparable contributions.

(2) Quantitative analysis of the pore network model indicated the following order of average pore and throat radii: SK42 > SS21 > SK21. SS21 displayed the widest throat radius distribution, whereas SK42 had the largest average throat radius but fewer developed throats. Connectivity analysis ranked pore-fracture connectivity and connection strength as SS21 > SK21 > SK42, with SS21 demonstrating superior connectivity and structural integrity

References

[1] Wang G, Han D Y, Qin X J, et, al. A comprehensive method for studying pore structure and seepage characteristics of coal mass based on 3D CT reconstruction and NMR[J]. Fuel, 2020, 281: 118735.

[2] Milliken K L, Rudnicki M, Awwiller D N, et al. Organic matter-hosted pore system, Marcellus Formation, Pennsylvania [J]. AAPG Bulletin, 2013, 97(2): 177-200.

[3] Dantas S, Struckhoff K C, Thommes M, et al. Phase behavior and capillary condensation hysteresis of carbon dioxide inmesopores[J]. Langmuir, 2019, 35(35): 11291-11298.

[4] Wen Z H, Wang Q, Yang Y P, et, al. Pore structure characteristics and evolution law of different-rank coal samples[J].Geofluids, 2021, 2021(4): 1-17.

[5] Li Z T, Liu D M, Cai Y D, et, al. Adsorption pore structure and its fractal characteristics of coals by N2 adsorption/desorption and FESEM image analyses[J]. Fuel, 2019, 257: 116031.

[6] Zhang G L, Ranjith P G, Fu X H, et al. Pore-fracture alteration of different rank coals: implications for CO2 sequestration in coal[J]. Fuel, 2021, 289: 119801.

[7] Wang X L, Pan J N, Wang K, et al. Characterizing the shape, size, and distribution heterogeneity of pore-fractures in high rank coal based on X-ray CT image analysis and mercury intrusion porosimetry[J]. Fuel, 2020, 282: 118754.

[8] Qin L, Li S G, Zhai C, et al. Changes in the pore structure of lignite after repeated cycles of liquid nitrogen freezing as determined by nitrogen adsorption and mercury intrusion[J]. Fuel, 2020, 267: 117214.

[9] Li Y T, Jiang Y D, Zhang B, et, al. Investigation on the pore characteristics of coal specimens with bursting proneness[J]. Scientific Reports, 2019, 9: 16518.

[10] Ju Y, Xi C D, Zhang Y, et al. Laboratory in situ CT observation of the evolution of 3D fracture networks in coal subjected to confining pressures and axial compressive loads: a novel approach[J]. Rock Mechanics and Rock Engineering, 2018, 51(11):3361-3375.

[11] Jing D J, Meng X X, Ge S C, et, al. Reconstruction and seepage simulation of a coal pore-fracture network based on CT technology[J]. Plos One, 2021, 16(6): e0252277.

[12] Li Y W, Yang Y F, Dong M Z, et, al. Effect of pore structure and capillary number on gas-water flow patterns in carbonate rocks[J]. SPE J, 2022, 27(04): 1895-1904.

[13] LI Yanhe, WANG Baoyu, LIU Shunxi, et al. Sedimentary Environment of Coal-bearing Strata in Pingdingshan Mining Area, Henan Province and Its Control on Coal Measure Gas Accumulation[J]. Acta Paleogeographica Sinica

[14] Zhai Yingquan, Li Meng, Pan Jienan, et al. Coal Science and Technology,2020,48(6):191-198.)

[15] Xu Yaobo. Analysis of Interference Between Layers in the Development of Coalbed Methane Wells and Discussion on Combined Production Methods: A Case Study of Shoushan No. 1 Mine in Pingdingshan [J]. Coalfield Geology and Exploration, 2021, 49(3): 112-117, 127.

[16] WANG Xianglong. Characteristics of structural coal porosity fractures and their controlling effect on permeability[D].Henan Polytechnic University, 2021.

[17] Zhu Q, Wang X, Zuo Y, et al. Numerical simulation of matrix swelling and its effects on fracture structure and permeability for a high-rank coal based on X-ray micro-CT image processing techniques[J]. Energy & Fuels, 2020, 34(9): 10801-10809.